remote sensing

MDPI

Article

Consistency of Vertical Reflectivity Profiles and Echo-Top Heights between Spaceborne Radars Onboard TRMM and GPM

Lei Ji [1], Weixin Xu [1,2,3,*], Haonan Chen [4] and Nana Liu [5]

[1] School of Atmospheric Sciences, Sun Yat-sen University, Zhuhai 519082, China; jilei0426@gmail.com
[2] Southern Marine Science and Engineering Guangdong Laboratory (Zhuhai), Zhuhai 519082, China
[3] Guangdong Province Key Laboratory for Climate Change and Natural Disaster Studies, Guangzhou 510275, China
[4] Department of Electrical and Computer Engineering, Colorado State University, Fort Collins, CO 80523, USA; haonan.chen@colostate.edu
[5] Department of Earth System Science, University of California Irvine, Irvine, CA 92697, USA; nana.liu@uci.edu
* Correspondence: xuwx25@mail.sysu.edu.cn

Abstract: Globally consistent long-term radar measurements are imperative for understanding the global climatology and potential trends of convection. This study investigates the consistency of vertical profiles of reflectivity (VPR) and 20-dBZ echo-top height (Topht20) between the two precipitation radars onboard the Tropical Rainfall Measuring Mission (TRMM) and Global Precipitation Measurement (GPM) satellites. Results show that VPR coincidently observed by the TRMM's and GPM's Ku-band radar agree well for both convective and stratiform precipitation, although certain discrepancies exist in the VPR of weak convection. Topht20s of the TRMM and GPM are consistent either for coincident events, or latitudinal mean during the 7-month common period, all with biases within the radar range resolution (0.1–0.2 km). The largest difference in the Topht20 between the TRMM's and GPM's Ku-band radar occurs in shallow precipitation. Possible reasons for this discrepancy are discussed, including sidelobe clutter, beam-mismatch, non-uniform beam filling, and insufficient sampling. Finally, a 23-year (1998–2020) climatology of Topht20 has been constructed from the two spaceborne radars, and the global mean Topht20 time series shows no significant trend in convective depth during the last two decades.

Keywords: TRMM; GPM; precipitation radar; vertical profiles of reflectivity; radar echo-top height; convection

Citation: Ji, L.; Xu, W.; Chen, H.; Liu, N. Consistency of Vertical Reflectivity Profiles and Echo-Top Heights between Spaceborne Radars Onboard TRMM and GPM. *Remote Sens.* **2022**, *14*, 1987. https://doi.org/10.3390/rs14091987

Academic Editors: V. Chandrasekar, Yingzhao Ma, Robert Cifelli and Seppo Pulkkinen

Received: 8 March 2022
Accepted: 18 April 2022
Published: 21 April 2022

1. Introduction

Convection is not only the major trigger of severe weather including extreme precipitation, large hail, intense lightning, damaging winds, etc. [1–5], but also plays an important role in the global circulations of water mass and energy [6,7]. Furthermore, intense convection with overshooting top is a major contributor to the exchange of water vapor and chemical species from the troposphere to the stratosphere [8–10]. Under global warming, the frequency and intensity of intense convective storms have increased over many regions around the world during the last few decades [11,12], and their increasing trends are projected to continue [13]. So far, the observed trends of intense convection are only based on observations of indirect convective proxies such as lightning and extreme surface precipitation [14–18]. Though passive satellite remote sensing measurements including Infrared and passive microwave provide useful information about the vertical development of convection, they display great uncertainty regarding storm heights because brightness temperature also depends on the surface emissivity, atmospheric temperature, and humidity [19–21]. Therefore, a globally consistent long-term dataset on the vertical structure of convective storms is crucial in better understanding the nature of intense convective storms

and quantifying their long-term trends in the future. The precipitation radars onboard the Tropical Rainfall Measuring Mission satellite (TRMM, operated from December 1997 to April 2015; [22]) and its successor, Global Precipitation Measurement (GPM, launched in February 2014 and in operation since then; [23]) mission, together provide nearly 25 years of three-dimensional (3D) radar measurements and are expected to collect convective observations for years to come. Obviously, the combined TRMM-GPM precipitation radar data will be a precious legacy for climate research regarding convective storms.

The TRMM-GPM precipitation radar data have been widely used to investigate the characteristics of various convective storms on both regional and global scales, including intense convection [6,24,25], extreme precipitation [26,27], mesoscale convective systems [28–31], and shallow or warm-rain precipitation systems [32]. Among many precipitation radar variables, the echo-top height of a certain reflectivity threshold is the most straightforward in representing how tall the convection develops [33,34]. For example, the 20-dBZ echo-top height represents the maximum height that the precipitation-size particles are lofted by the updraft [21,35]. This proxy has often been considered an indicator of either deep convective cells or shallow convection [36–39], including tropical cyclone hot towers [40,41]. It has also been applied in identifying convection overshooting the tropopause, which not only promotes the troposphere-stratosphere transportation of water vapor and chemical species [8,9], but also generates strong local turbulence above the precipitation cloud top that threatens aviation safety [42]. Meanwhile, the 20-dBZ echo-top height over the tropical ocean shows significant seasonal and intraseasonal variations associated with summer monsoon [25] and Madden–Julian Oscillation [43], as well as diurnal variations [44]. However, almost all the related analyses were carried out using observations from the TRMM or GPM solely, and the benefits of combining the TRMM and GPM data for an extended convective climatology have rarely been explored. Nevertheless, the consistency of the vertical precipitation structures, including echo-top heights between the TRMM/GPM Ku-band radars, is still unknown.

Surface precipitation estimates from the TRMM/GPM Ku-band radars agreed well with each other [45,46], although certain discrepancies between vertical precipitation profiles were also reported [47]. Takahashi and Fujinami [48] disclosed an increasing frequency of heavy precipitation along the Meiyu-Baiu front over the last 22 years with the combined surface precipitation from the TRMM and GPM. The above comparison and application of Ku-band radar observations from the TRMM and GPM mainly focus on surface precipitation. Yet, as an important proxy of the intensity of precipitating clouds [6,21], the coherence of precipitating cloud top heights between both radars have not been evaluated. Although the tallest storms do not always correspond to the heaviest rainfall rates [26], the contribution of total precipitation and natural disasters are mainly connected to precipitation clouds with high tops [29]. In consideration of the updated radar sensitivity and algorithms as well as their more than two decades of observations of global precipitating clouds in total [49], the goals of this study are: (1) examine the consistency of vertical radar profiles and 20-dBZ echo-top heights from the TRMM/GPM Ku-band radars; (2) construct and examine the extended climatology of 20-dBZ echo-top heights through combining measurements from the two spaceborne radars.

The structure of this study is organized as follows: Section 2 introduces the data preparations of Ku-band radars from both satellite platforms and the details of the three-step methodology for the investigation. Section 3 depicts the results from each step according to the investigation methodology on different spatiotemporal scales. Section 4 includes a short discussion about the reasons for the long-term climatological difference of echo-top height between the two Ku-band precipitation radars. The last section concludes the findings of this study.

2. Data and Methods

2.1. Datasets

The datasets from the TRMM 2A.PR (TRMM_PR, hereafter) version 8 (V8) and the Normal scan Swath (NS) of GPM 2ADPR (GPM_KuPR, hereafter) version 06A (V06A) are

employed in this study. The attenuation of Ku-band radar reflectivity caused by heavy precipitation and cloud water has been well corrected [50,51]. The TRMM_PR V8 and GPM_KuPR V06A have been calibrated with the same calibrator and share a similar data-processing algorithm [52]. Therefore, it is fair to use them for comparison. Note that the newest version of the GPM (V07) dataset released on 6 December 2021, is not used here, because its corresponding version of the TRMM dataset (possibly TRMM V9) has not been released (https://www.eorc.jaxa.jp/GPM/en/archives.html, accessed on 10 April 2022). The TRMM_PR V8 and GPM_KuPR V06A share nearly the same data specifications, especially after the orbit boost of the TRMM in August 2001 (Table 1). Note that the TRMM PR has a slightly finer horizontal resolution before the boost (4.3 km) than after (5 km). Additionally, GPM_KuPR is expected to have higher sensitivity and thus lower minimum detectable reflectivity than the TRMM_PR [51,53]. Both the TRMM_PR and GPM_KuPR have the same vertical resolution, as the range resolution in the TRMM_PR V8 has been updated to 0.125 km with 176 vertical levels after using the same data processes as the GPM_KuPR V06A [54]. It should be noted that the original range resolution of the TRMM_PR is 0.25 km [23].

Table 1. Main nominal specifications of the TRMM_PR V8 and GPM_KuPR V06A.

Instrument	TRMM PR V8	GPM KuPR V06A
Frequency (GHz)	13.8	13.6
Altitude (km)	403 (350) †	407
footprint	49	49
Incidence angle (°)	17	17
Inclination angle (°)	35	65
Horizontal resolution (km)	5 (4.3) †	5
Swath width (km)	247 (215) †	245
Vertical resolution (m)	125	125
Number of vertical levels	176	176
Minimum detectable reflectivity (dBZ) [and rain rate (mm h^{-1})]	18 [0.5]	18 [0.5]

† Specifications before the TRMM's orbit boost in August 2001 are noted in parentheses.

The near-surface radar reflectivity (i.e., nearSurfdBZ) is used to select pixels with detectable surface precipitation. Considering the higher sensitivity of the GPM_KuPR than that of the TRMM_PR [51,53], the minimum reflectivity threshold of 13 (18) dBZ for the GPM_KuPR (TRMM_PR) is adopted for the data quality-control to eliminate unreliable data, which only account for less than 0.005% of the total samples. The vertical reflectivity profiles are attenuation-corrected (i.e., zFactorCorrected), and the 20-dBZ echo-top height (i.e., Topht20) is defined as the maximum height of 20-dBZ reflectivity within each profile.

Samples are further classified by land surface types and rain types. Only land and ocean surface types are considered since samples belonging to other surface types (e.g., coast) are rare. Precipitation samples are separated into convective and stratiform types using the rain type classification products from the TRMM_PR and GPM_KuPR. The GPM DPR provides two kinds of rain type products; one is based on single frequency (Ku_only or Ka_only), and the other uses dual frequency (Ku and Ka). To be consistent with the TRMM_PR, the single frequency (Ku) product is used here. The single frequency rain type algorithm consists of both the vertical profiling method (considering vertical precipitation structures) and the horizontal pattern method (based on horizontal precipitation gradients) [55,56]. A side-lobe peak misrecognition and a heavy ice precipitation problem have been fixed in the TRMM_PR V8 and GPM_KuPR V06A [51,57]. Although there are uncertainties in rain type classification, the misclassification rate is quite low and hence has negligible impact on the following analyses [51].

2.2. Methodology

The study region is constrained to the TRMM-GPM overlapped latitudes from 36.5°S to 36.5°N. The investigation consists of three steps, called coincident comparison, overlapping period comparison, and extended climatology.

Coincident comparison: only pixels from the TRMM_PR and GPM_KuPR that matched temporally and spatially (so-called coincident) are included, aiming to evaluate their consistency in detecting the same precipitation events. Coincident event (pixel) pairs between the TRMM_PR and GPM_KuPR are sought out during their common in-service period from 8 March to 7 October 2014. Since the TRMM satellite began to descend on 8 October 2014, the measurements of the TRMM_PR after this time are excluded in this study. The vertical profiles of reflectivity (VPR), as well as the Topht20s, are further screened out from coincident precipitation events with nearSurfdBZ above 18 dBZ, so that comparisons between the TRMM_PR and GPM_KuPR are conducted on the exact same samples. Here, a coincident event pair is defined as two-radar pixels that are within a 2.5 km distance and a 15 min observational time interval [45,46,58]. These time and distance interval thresholds are defined based on sensitivity experiments. Specifically, the Pearson correlation coefficient (PCC) and the sample numbers of coincident event pairs are calculated as a function of time and distance interval (Figure 1). Obviously, the increase of the PCC is included in the compensation for the decrease of the sample numbers. The selection criteria (2.5 km and 15 min spatiotemporal intervals) have the premium balance between the PCC (0.83) and sample number (70% of the total samples of sensitivity experiments).

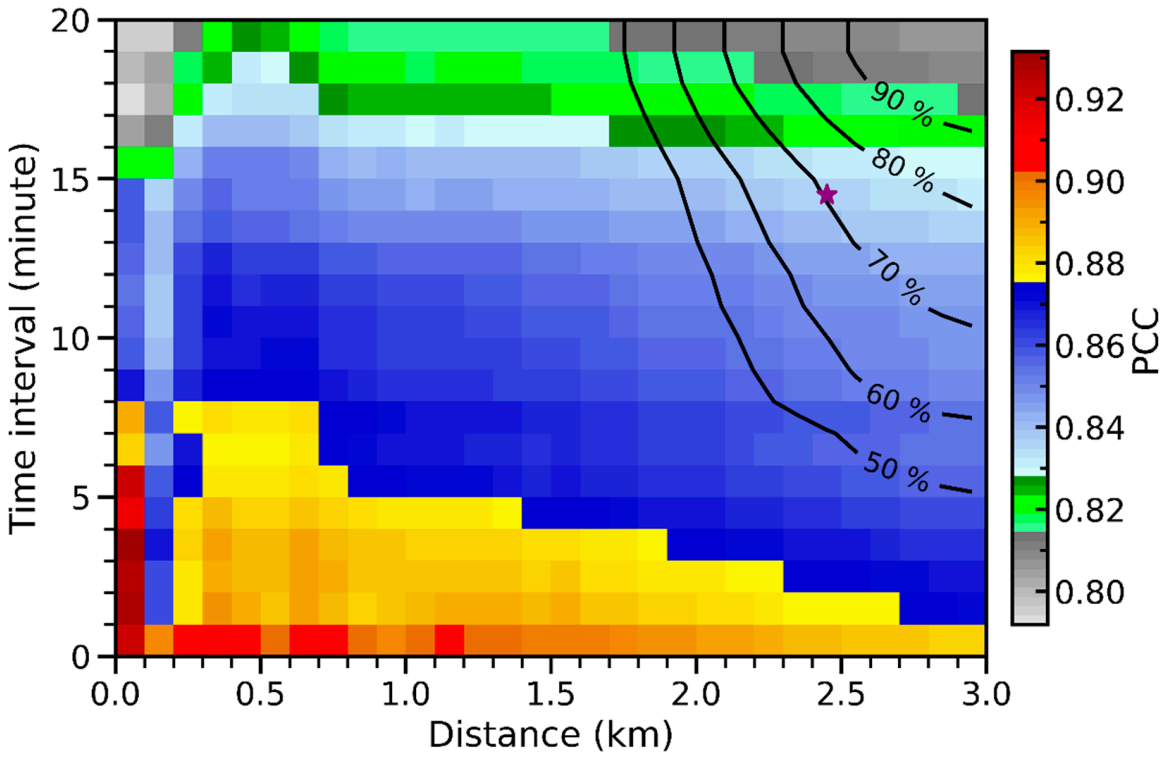

Figure 1. The matrix of Pearson correlation coefficients (PCCs, shaded) and the percentage of coincident Topht20s (contours, begins at 50%), as a function of distance and time interval between the TRMM_PR and GPM_KuPR. The resolutions of distance and time interval are 0.1 km and 1 min, respectively. The purple star represents the criteria in this study.

Overlapping period comparison: all Topht20 pixels (either coincident or not) from each radar during their overlapping in-service period (March to October 2014) are included. This comparison aims to examine the consistency between the TRMM_PR and GPM_KuPR of the Topht20 of convection occurring within the same overlapping period. The *p*_value

estimated by the Student's T-test approach is adopted to evaluate the significant difference (when p_value < 0.05) in Topht20 between the two radars.

Extended climatology: all Topht20 pixels from the TRMM_PR between 1 January 1998, and 7 October 2014, and from the GPM_KuPR between 8 March 2014, and 31 December 2020, are combined for an extended time series. This is one of the important outcomes derived from this study, which will be very useful for future climate research, such as research into interdecadal (e.g., long-term trend) or interannual (e.g., El Niño-Southern Oscillation (ENSO)) variation of convection over a region or the globe.

3. Results

3.1. Coincident Precipitation Events Comparison

There are 3,929,231 coincident pixel pairs (either raining or not) from the TRMM_PR and GPM_KuPR, including 98,832 precipitation VPR and 97,619 Topht20 events. Samples over the ocean are more frequent than those over land (Figure 2). Coincident events are more concentrated over the deep tropics (10°N–20°N or 10°S–20°S), where convection is the most frequent. Fewer coincidences are found near the equator, where orbital satellites have the largest revisiting time intervals. More coincident events are found in the Northern Hemisphere than in the Southern Hemisphere, mainly because it is a wet (dry) season in the Northern (Southern) Hemisphere during the analyzing period (March to October). Coincident Topht20s are somewhat evenly distributed over rainy regions in the tropics, such as the Intertropical convergence zone (ITCZ), the Pacific-Indian Ocean warm pool, the Asian Monsoon, and the South American Monsoon.

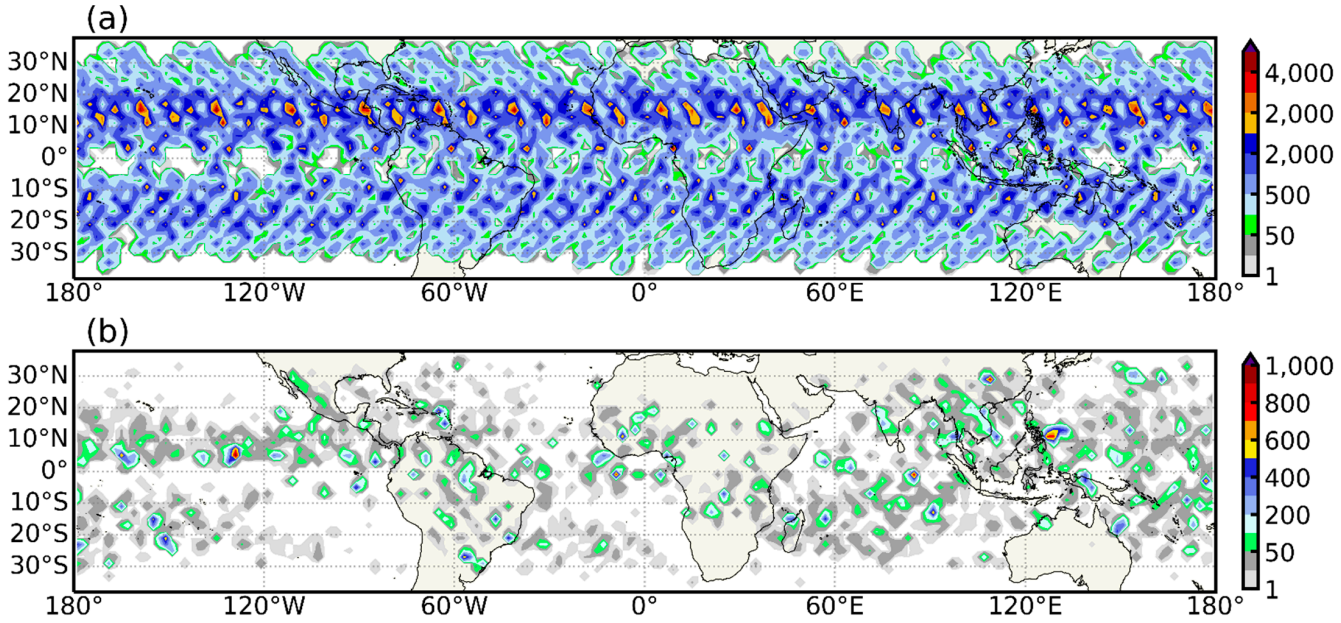

Figure 2. Global distribution of coincident events resampled to a spatial resolution of 2° × 2°. (**a**) All coincident events (with and without surface precipitation); (**b**) coincident Topht20s (with surface precipitation).

Figure 3 shows a precipitation system over the Northwest Pacific Ocean (to the east of the Philippines) coincidently observed by the TRMM_PR and GPM_KuPR on 22 March 2014. The time interval between the TRMM_PR and GPM_KuPR is about 4 min. The near-surface precipitation distributions between the two radars are nearly identical within the overlapping region, and the heavy precipitation centers (nearSurfdBZ above 40 dBZ) also match perfectly (Figure 3a,b). A vertical cross-section through the most intense convective cores is further drawn (Figure 3c,d). Again, the two radars share very similar vertical structures from many perspectives, such as a bright-band (near 5 km), a convective tower

(>12 km), uneven echo-top heights near 7–8 km, etc. Of course, there are some notable differences that may come from observing the time interval between the two radars (the GPM_KuPR is 4 min earlier). Taking the deepest convective core (300–350 km from point A) as an example, the GPM_KuPR shows both a higher radar reflectivity tower (e.g., 20 dBZ echo-top height) and heavier precipitation below the freezing level than the TRMM_PR. This is possibly because the GPM_KuPR observed the peak intensity of the convective core, and the TRMM_PR detected the slightly weakening precipitation core several mins later. Besides, a 1–2 km vertical layer of weak reflectivity (grey regions with reflectivity <20 dBZ) on the top of precipitation is shown in the GPM_KuPR but not the TRMM_PR, which is due to the higher sensitivity of the GPM_KuPR [51,53].

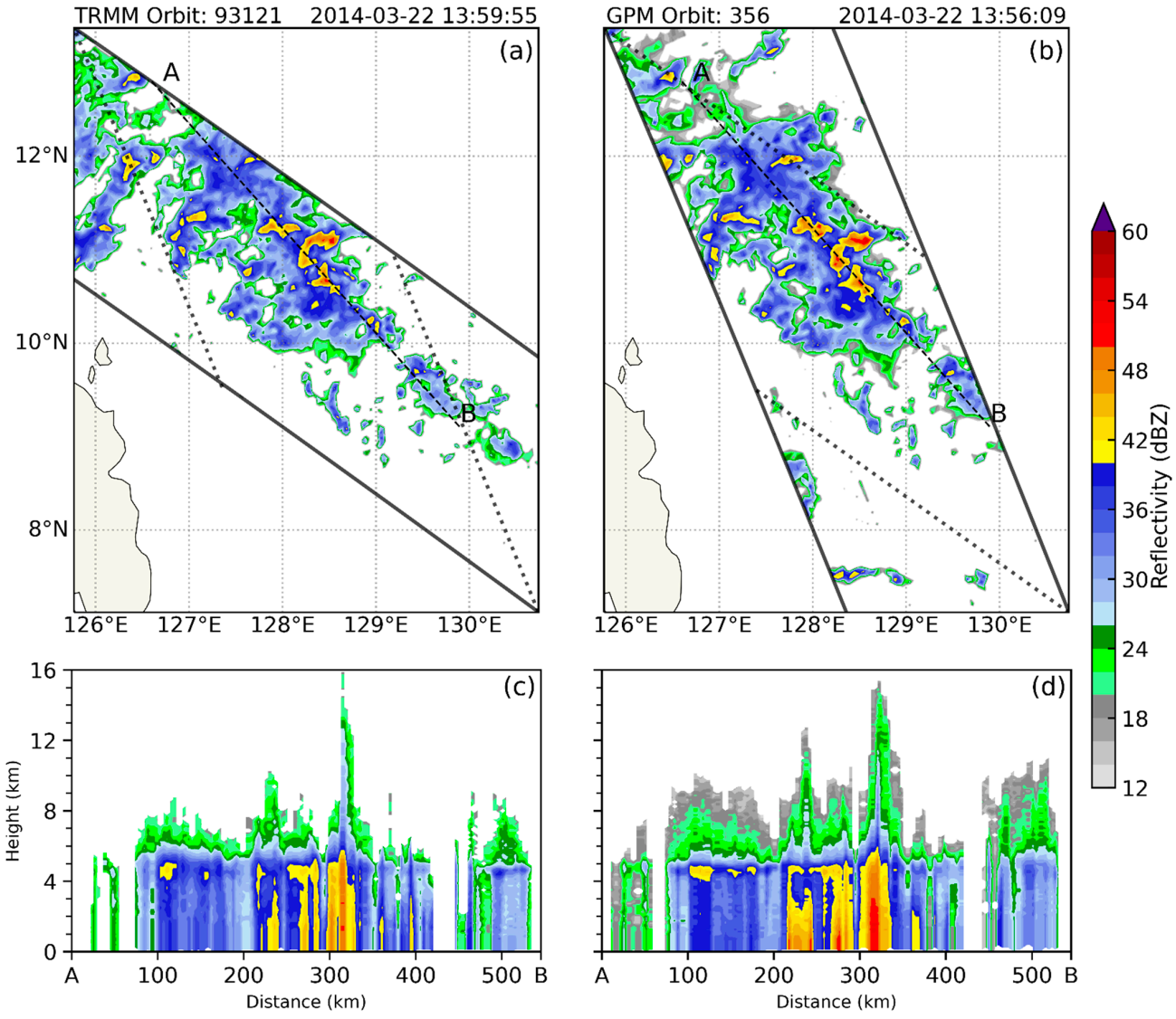

Figure 3. A precipitation system observed by the TRMM_PR (left column, orbit #93121, at about 14:00 UTC) and GPM_KuPR (right column, orbit #356, at about 13:56 UTC) on 22 March 2014. (**a**,**b**) The nearSurfdBZ and (**c**,**d**) the VPR (corresponding to the dashed line highlighted by points A and B). The solid lines represent the orbit edges of the TRMM_PR/GPM_KuPR in (**a**,**b**) and vice versa for the dotted lines. The coincident regions are highlighted within both solid and dotted lines.

Figure 4 shows the composited vertical profiles of coincident precipitation VPR as a function of percentile and precipitation type over land and ocean. When all precipitation types are included, VPR from the TRMM_PR and GPM_KuPR are close to each other,

with a difference of <0.5 dBZ at all altitudes (Figure 4a,d). The GPM_KuPR VPR still show reflectivity values smaller than 18 dBZ, due to the higher radar sensitivity of the GPM_KuPR. VPR between the TRMM_PR and GPM_KuPR also agree well after being further separated into convective and stratiform precipitation types (the second and third columns in Figure 4). The convective VPR show larger differences between the two radars (the second column), while the stratiform VPR match perfectly (the third column). Except in Figure 4b, the median convective VPR between two radars are the closest. GPM_KuPR shows larger reflectivity values for the moderate-to-deep precipitation VPR (75% and 95%). For the convection over land (Figure 4b), the GPM_KuPR is almost higher than the TRMM_PR at each altitude through all precipitation levels. The largest discrepancy is up to 2 dBZ near 3 km for median VPR. Overall, the differences in VPR between the two radars are acceptable (mostly <0.5 dBZ), as they are not perfectly matched in time and space.

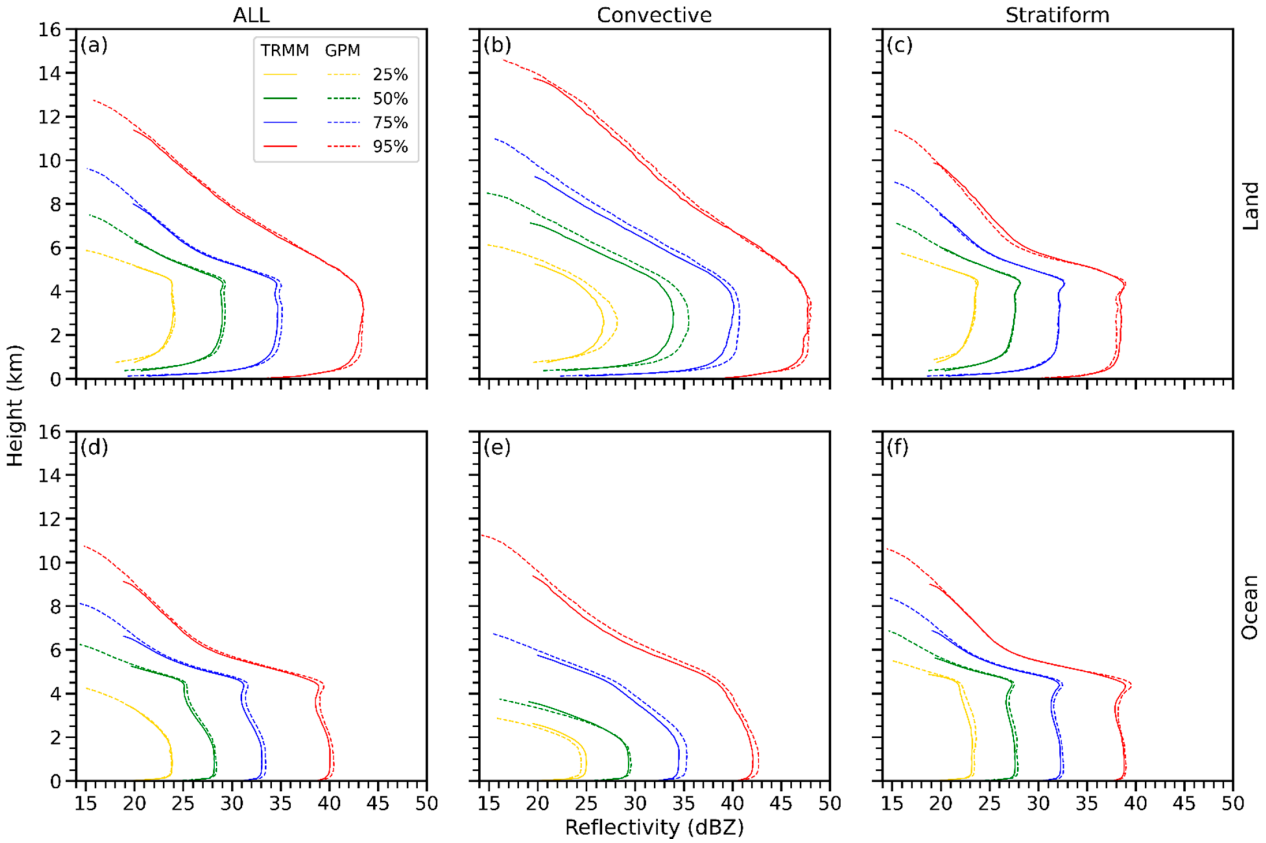

Figure 4. The coincident precipitation vertical profiles of reflectivity from the TRMM_PR (solid) and GPM_KuPR (dashed) in percentiles of 25% (yellow), median (green), 75% (blue), and 95% (red) over (**a**–**c**) land and (**d**–**f**) ocean. VPR are subdivided by ALL (first column), convective (second column), and stratiform (third column) rain types with a time interval of up to 15 min.

Since this study focuses on the Topht20, analyses hereafter will be on Topht20. Figure 5 shows the distribution (density) of coincident Topht20 from the GPM_KuPR (x-axis) versus the TRMM_PR (y-axis), as a function of land/ocean surface types and convective/stratiform rain types. Generally, Topht20 agrees well between the two radars, i.e., high sample density concentrates mainly along the diagonal line. When all kinds of Topht20 are considered, their Pearson correlation coefficients (PCCs) are quite high (around 0.8), and their biases are only 0.1–0.2 km, which is within the range resolution of both radars (Figure 5a). Topht20 over the ocean shows smaller difference (bias = 0.14 km) between GPM_KuPR and TRMM_PR (Figure 5c) than over land (bias = 0.25 km, Figure 5b). Convective precipitation over land shows the largest bias (0.34 km) on Topht20 between the two radars (Figure 5e), while its counterpart over the ocean displays the best PCC and the lowest bias (Figure 5f). This is

possibly because convective cells over land develop/move more rapidly than stratiform precipitation or convection over the ocean. However, the biases of all subgroups are lower than the original vertical resolution of TRMM_PR (except for the convective rain type over land). In short, TRMM_PR and GPM_KuPR show great consistency in detecting the Topht20 of various types of precipitation over both land and ocean.

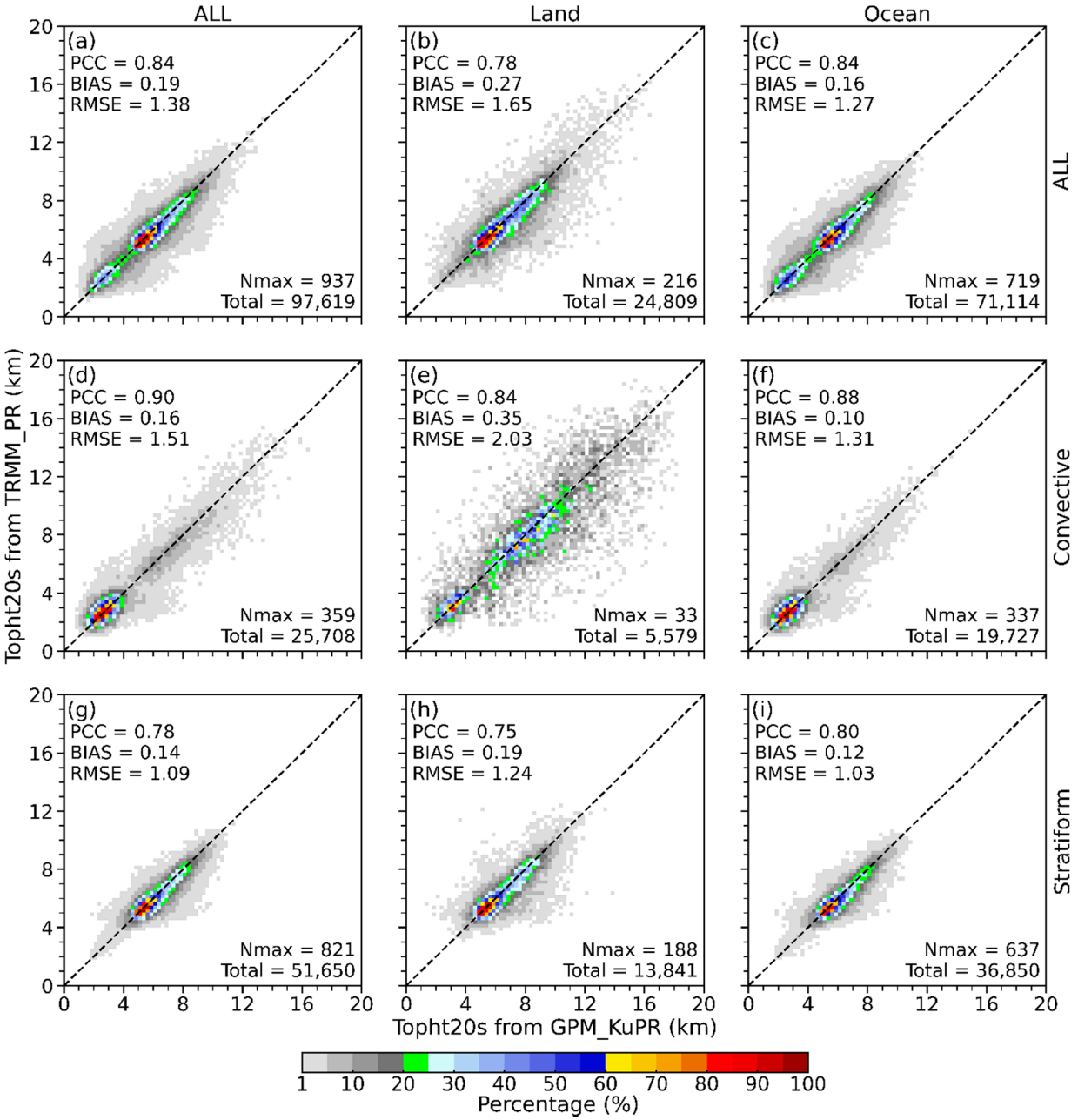

Figure 5. Two-dimensional density distributions of coincident Topht20 from the TRMM_PR (y-axis) and GPM_KuPR (x-axis) with a statistical grid resolution of 0.25 km × 0.25 km. Sub-groups are classified by rain types in rows ((**a**–**c**) ALL, (**d**–**f**) Convective, and (**g**–**i**) Stratiform) in rows and land surface types ((**a**,**d**,**g**) ALL, (**b**,**e**,**h**) Land, and (**c**,**f**,**i**) Ocean) in columns. The Pearson correlation coefficient (PCC), bias (GPM_KuPR−TRMM_PR, BIAS), and the root-mean-square error (RMSE) are provided. The maximum and total sample number in each grid are noted by Nmax and Total, respectively. Grid densities (shaded) are normalized by dividing the grid sample numbers by the Nmax in each panel.

The probability distribution functions (PDFs) of coincident Topht20 from the TRMM_PR and GPM_KuPR are further constructed as a function of altitude (Figure 6). Again, the PDFs of coincident Topht20s are fairly well matched between the two radars, in terms of both magnitude and vertical structure. The stratiform precipitation shows a dominant peak (at 5.5 km altitude) near or slightly above the freezing level over both land and ocean (blue lines). The convective precipitating clouds exhibit double peaks at 3.5 km and 7 km over land (2.6 km and 5.8 km over the ocean), associated with the shallow and moderate-to-deep convective modes widely recognized in the tropics [39,43]. Subtle differences are found when Topht20 PDFs are separated into convective and stratiform precipitation types. The TRMM_PR shows a higher frequency of shallow convective precipitation (<4 km) but a lower frequency of moderate-to-deep convection (>7 km) over both land and ocean.

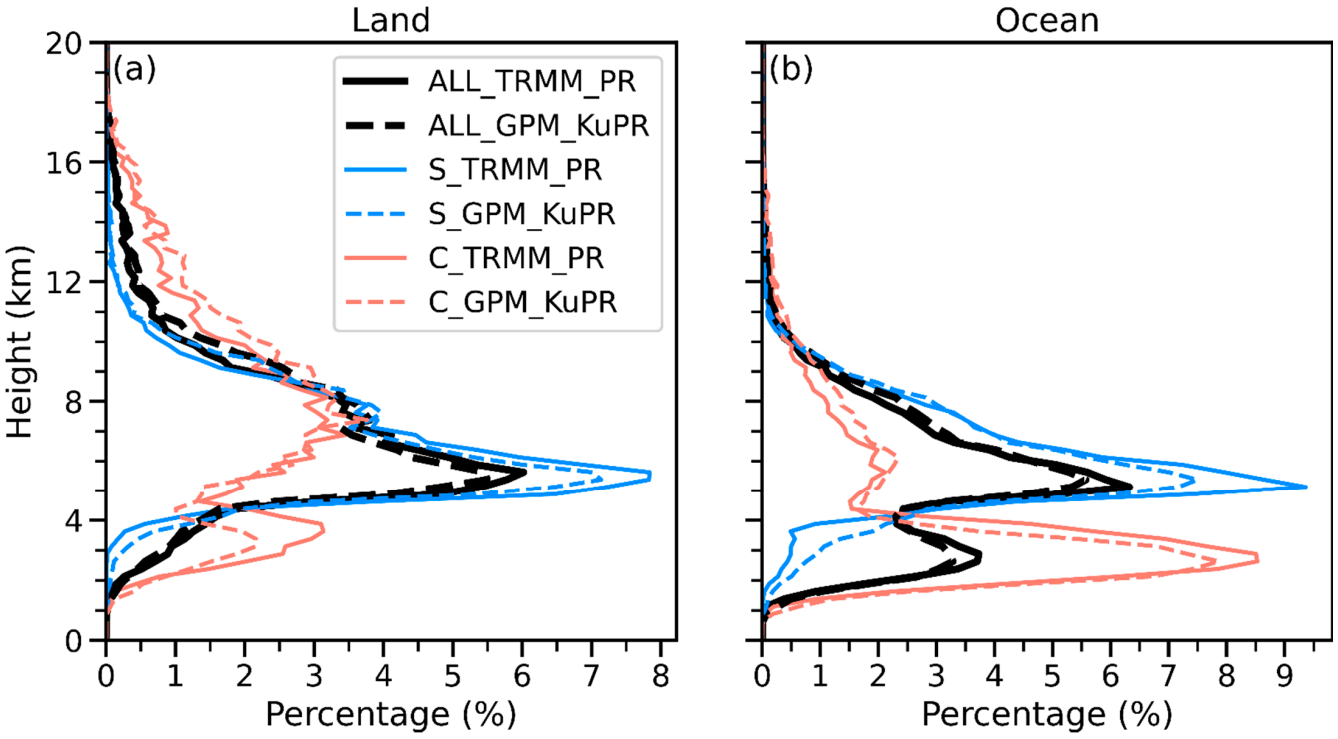

Figure 6. The probability distribution functions (PDFs) of coincident Topht20s from the TRMM_PR (solid lines) and GPM_KuPR (dashed lines) over (**a**) land and (**b**) ocean. Black, blue, and red lines represent all, stratiform, and convective rain types, respectively.

3.2. Overlapping Period Comparison

All Topht20 samples from the TRMM_PR and GPM_KuPR during their common operation period are analyzed in this section. There are 7.0 (34.2) and 4.6 (17.5) million Topht20 samples within the research region over land (ocean) from the TRMM_PR and GPM_KuPR, respectively. The sample ratio of convective precipitation to stratiform precipitation is about 1:2.9 (1:1.8) over land (ocean) for both radars.

The PDFs of the Topht20 during the overlapping period as a function of altitude are shown in Figure 7. They show very similar vertical structures as coincident Topht20 PDFs. However, shallow convection (red curves under 4 km in Figure 7) accounts for a larger fraction during the overlapping period than the coincident events (red curves under 4 km in Figure 6) over both land and ocean. This is possibly because a large amount of the short lifecycle of shallow convection [59] has a low chance of being detected by two spaceborne radar platforms coincidently. The Topht20 PDFs of the TRMM_PR and GPM_KuPR during the overlapping period agree even better than those of coincident events, likely due to a much larger sample. The Topht20 PDFs of "ALL" and stratiform rain types are perfectly overlapping over both land and ocean. The exception exists around 4 km over ocean (black

curves in Figure 7b) where the Topht20 PDF of the TRMM_PR is higher than that of the GPM_KuPR. Besides, the Topht20 of convective precipitation over land shows some small differences between the TRMM_PR and GPM_KuPR.

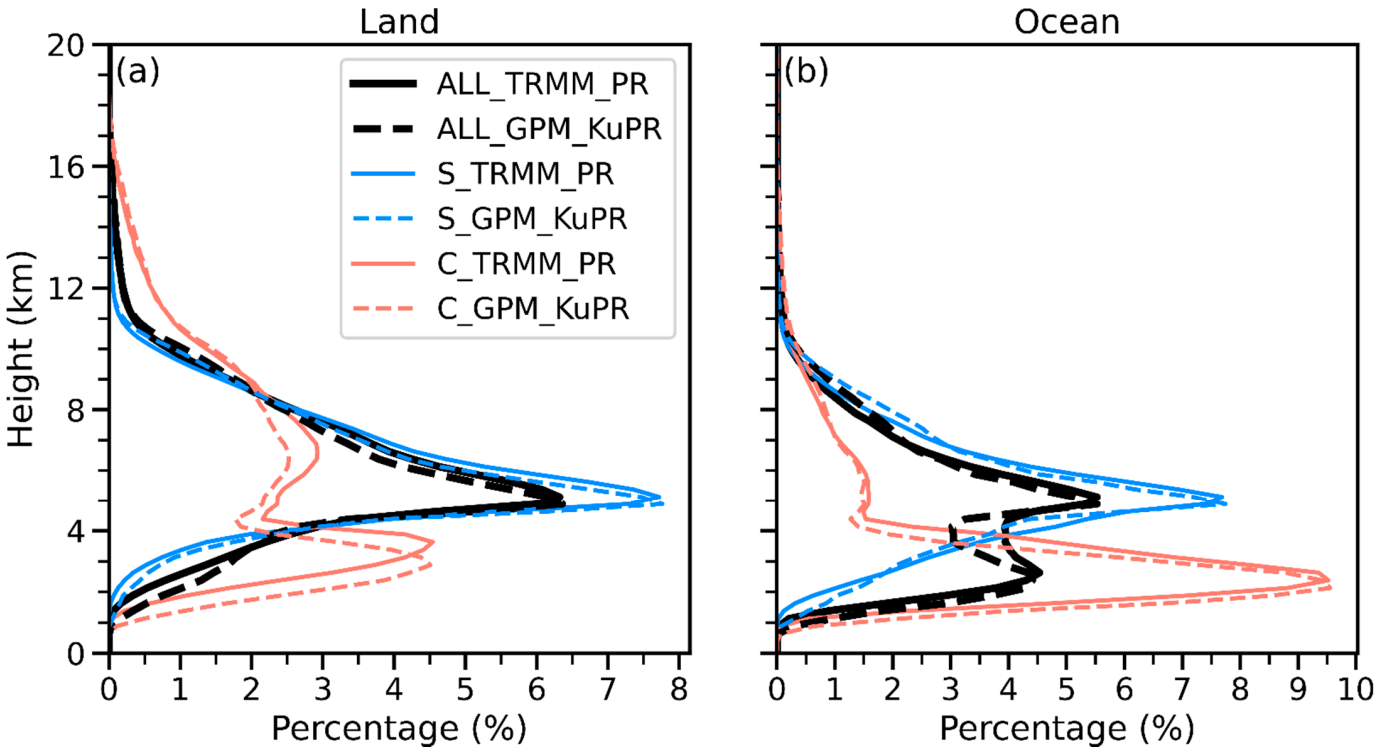

Figure 7. Same as Figure 6, but for the PDF of Topht20 during the overlapping period over (**a**) land and (**b**) ocean.

Figure 8 shows the latitudinal distributions of Topht20 during the overlapping period of different rain types over land and ocean. In general, the latitude-mean Topht20s over most latitudes agree well between the two radars. The difference of the mean Topht20s in the Northern Hemisphere (0.1 km) is smaller than that in the Southern Hemisphere (0.2 km). However, a minimum p_value of 0.138 for the mean value of all subsets in Figure 8 via the Student's t-test method suggests that there is no significant difference of Topht20s between the two radars.

Topht20 samples are further categorized into shallow (Topht20 < 4 km), moderate (4 km $\leq$ Topht20 < 8 km), and deep (Topht20 $\geq$ 8 km) groups (Figure 9). It is worth noting that only tiny differences of mean value are found from moderate and deep convection events (smaller than 0.03 km) with corresponding standard deviation almost overlapping, but the means from shallow precipitation are notably lower from the GPM_KuPR than from the TRMM_PR (around 0.2 (0.15) km over land (ocean)) throughout the latitudinal ranges. This may be related to the effects of the sidelobe clutter from the GPM_KuPR [47,60] and the beam-mismatch from the TRMM_PR [61,62]. Although the up-to-date method has been applied to remove sidelobe clutter from the GPM_KuPR [60], the high sensitivity of the GPM_KuPR still causes this effect at specific angle bins and altitudes [47] which could result in the misidentification of precipitation. Meanwhile, the beam-mismatch from the TRMM_PR after the orbit boost could lead to the missing of shallow precipitation because of the degradation of the signal-to-noise ratio [61,62]. This also explains why the Southern Hemisphere shows greater uncertainty on Topht20s than the Northern Hemisphere (Figure 8), as shallow precipitation dominates most areas in the Southern Hemisphere such as the cold tongue and the southern Atlantic Ocean [6,29].

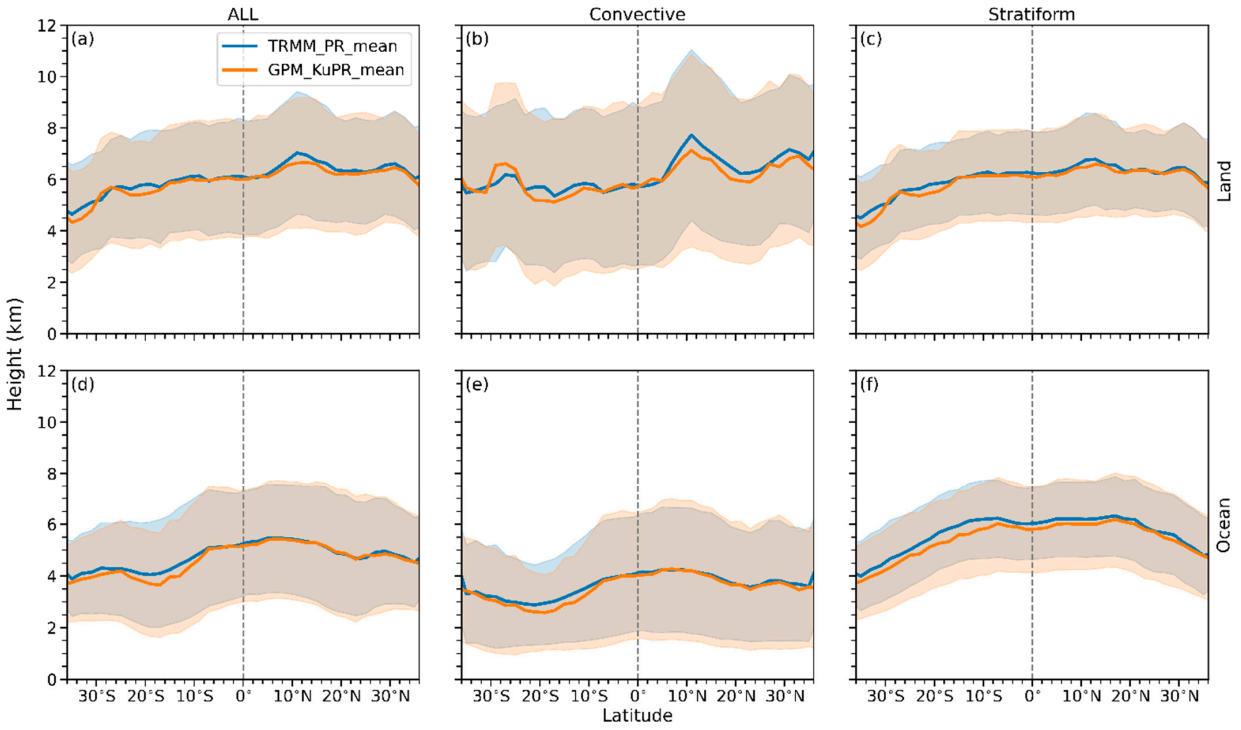

Figure 8. The mean (lines) and standard deviation (shades) of Topht20 during the overlapping period as a function of latitudes (2° resolution) from the TRMM_PR (blue) and GPM_KuPR (red) over (**a**–**c**) land and (**d**–**f**) ocean. Samples are subdivided by ALL (first column), convective (second column), and stratiform (third column) rain types.

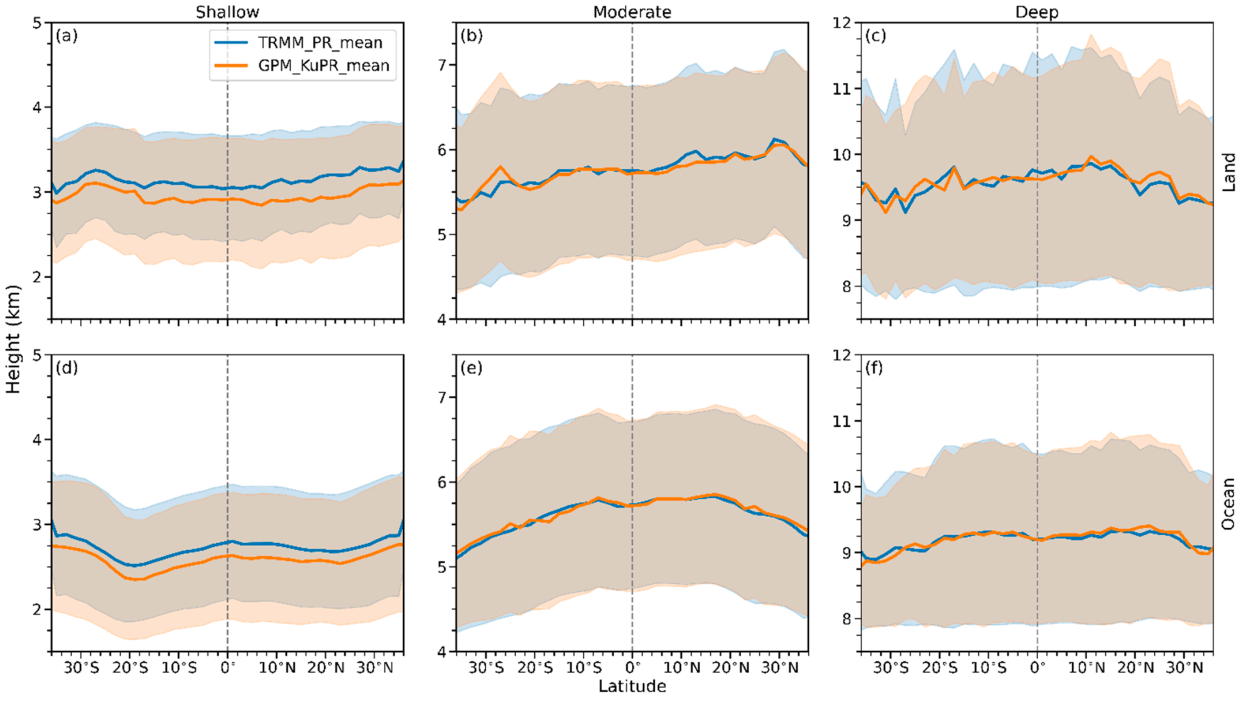

Figure 9. Same as Figure 8, but for shallow (Topht20 < 4 km, first column), moderate (4 km ≤ Topht20 < 8 km, second column), and deep (Topht20 ≥ 8 km, third column) convection events over (**a**–**c**) land and (**d**–**f**) ocean.

3.3. Extended Long-Term Climatological Comparison

Figure 10 shows the monthly mean Topht20 time series from the TRMM_PR and GPM_KuPR during 1998–2020. Generally, there is no evident trend on Topht20 over various latitude bands from the TRMM era (1998–2014) and the GPM era (2014–2020) with an annual mean difference of less than 0.15 km between these two periods. Of course, it warrants further study in investigating the long-term Topht20 variations on the regional scale or from the perspective of certain climate regimes. During the common in-service period (March–October, 2014), the monthly-mean Topht20s (M_Topht20s) from both radars are very consistent over ocean, but there are certain discrepancies over land (mostly 0.2–0.3 km). The *p*_values (via the Student's T-test) of Topht20s from the TRMM_PR and GPM_KuPR are higher than 0.175, indicating that the variations of M_Topht20s are not statistically significant between the TRMM_PR and GPM_KuPR. The maximum difference appears over the subtropics in the Southern Hemisphere (about 0.7 km), where Topht20 samples are smaller and dominated by shallow convection.

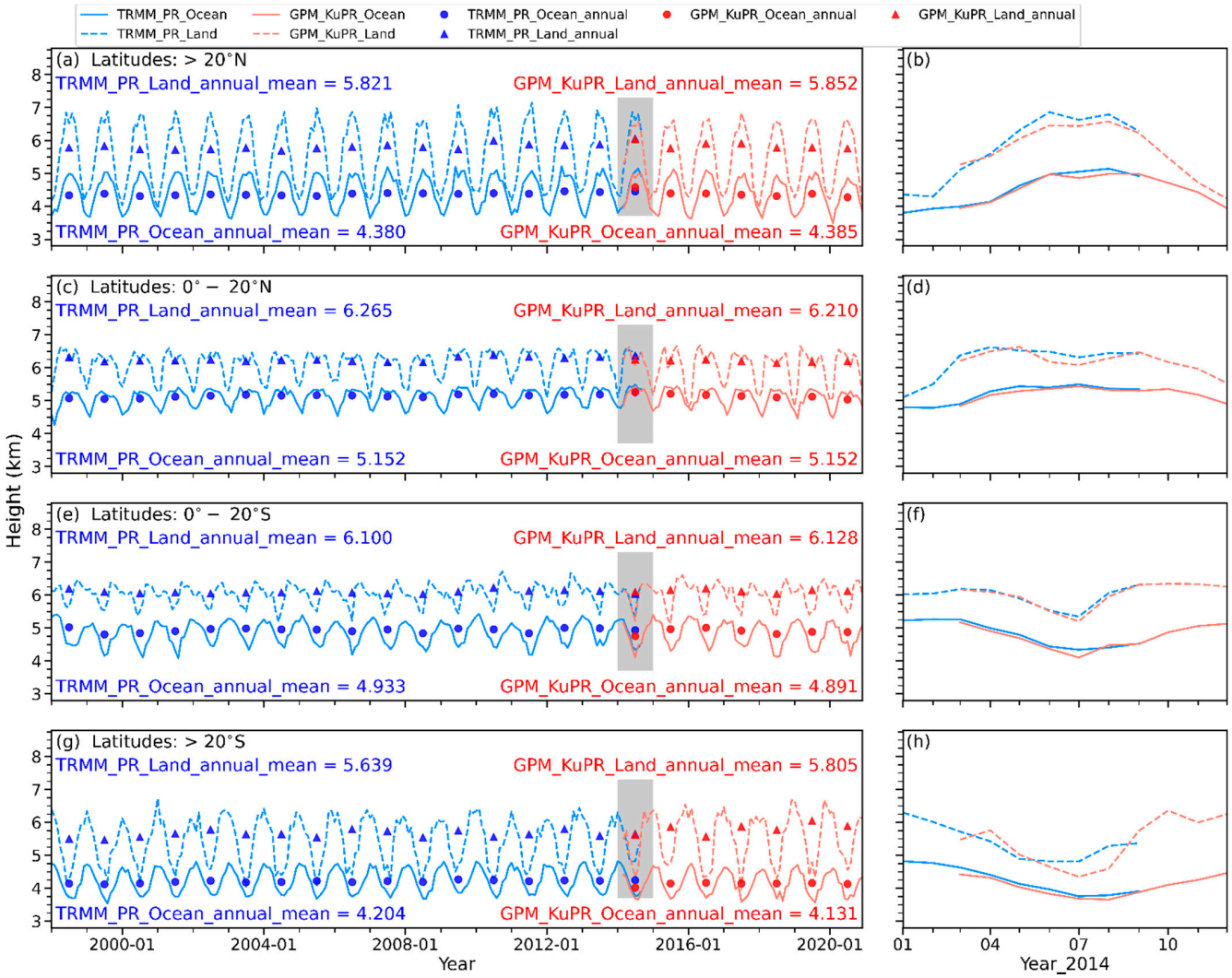

Figure 10. Time series (1998–2020) of monthly averaged Topht20 from the TRMM_PR (blue lines) and GPM_KuPR (red lines) within the latitudinal belt (**a**,**b**) greater than 20°N, (**c**,**d**) between 0°–20°N, (**e**,**f**) between 0°–20°S, and (**g**,**h**) greater than 20°S over land (dashed lines) and ocean (solid lines). Panels in the right column highlight the details in 2014. The annual mean Topht20s are denoted by triangles and dots over land and ocean, respectively. The mean values of Topht20s over land (ocean) from the TRMM_PR (1998–2014) and GPM_KuPR (2014–2020) are marked by text.

Figure 11 displays the global distribution of the mean Topht20 by combining Topht20s from the TRMM_PR (1998–2014) and GPM_KuPR (2014–2020), and the difference between the two radars. The mean Topht20s over land are mostly above the freezing level (>6 km); much higher than those over the ocean (Figure 11a). The highest mean Topht20s (>8 km) occur over high terrain such as the Tibet Plateau and the Andes Mountains, where the actual precipitation top from the ground in these regions may be only 5–6 km. Elevated Topht20s also occur in arid regions including the Sahara Desert in Africa and the West Jaz Mountains in the Arabian Peninsula, likely due to strong surface heating over these regions. Topht20s over the Pacific-Indian warm pool or the ITCZ oceans are around 4–5 km, while they are extremely shallow (2–3 km) over the cold tongue in the southeast Pacific Ocean and southern Atlantic Ocean. Note that this climatological mean is conditional on precipitation with detectable echo tops (20 dBZ). In other words, it only represents how high the convection will reach when it occurs but not how frequently the convection happens. This is possibly why the well-known hotspots of extreme convection are not shown in this distribution map, as shallow convection may also be frequent over those regions.

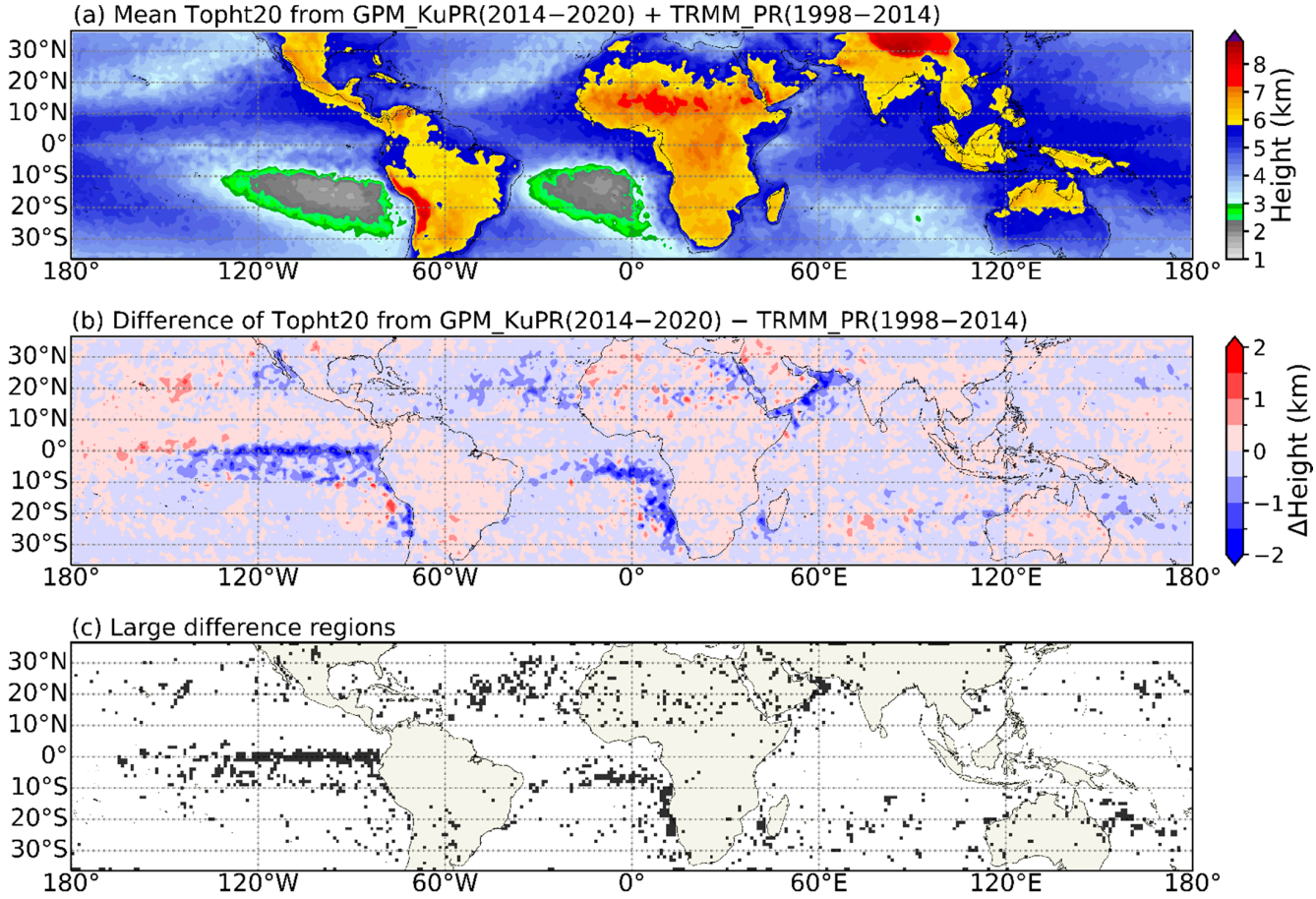

Figure 11. Global distribution (1° × 1°) of (**a**) mean Topht20 from the combination of the TRMM_PR and GPM_KuPR during 1998–2020, (**b**) Topht20 difference of the GPM_KuPR (2014–2020) minus TRMM_PR (1998–2014), and (**c**) large-difference grids (black points) with absolute difference value greater than its standard deviation and 0.5 km threshold.

To further quantify the climatological consistency of Topht20 between the TRMM_PR and GPM_KuPR, the standard deviation of the TRMM_PR (SD_PR) is calculated in each grid box. Grid boxes with Topht20 difference greater than the SD_PR and 0.5 km threshold are thought to be significant and are labeled with black points in Figure 11c; these account for only 6% of the total grids (1519). The majority of these large-difference grids are located in

shallow convective regions (averaged Topht20 < 4 km). As pointed out earlier (Section 3.2), the largest discrepancy in Topht20 between the two radars appears in detecting shallow convection, likely due to the issues of sidelobe clutter in the GPM_KuPR and beam-mismatch in the TRMM_PR. Moreover, shallow convection is usually isolated in nature [59], which may easily cause non-uniform beaming issues and increase the uncertainty of estimating the radar echo-top height (Topht20). Last but not least, significant difference occurs in grids with relatively limited samples (Figure 12); therefore, the insufficient sampling also contributes to the discrepancy in Topht20 between the GPM_KuPR and TRMM_PR.

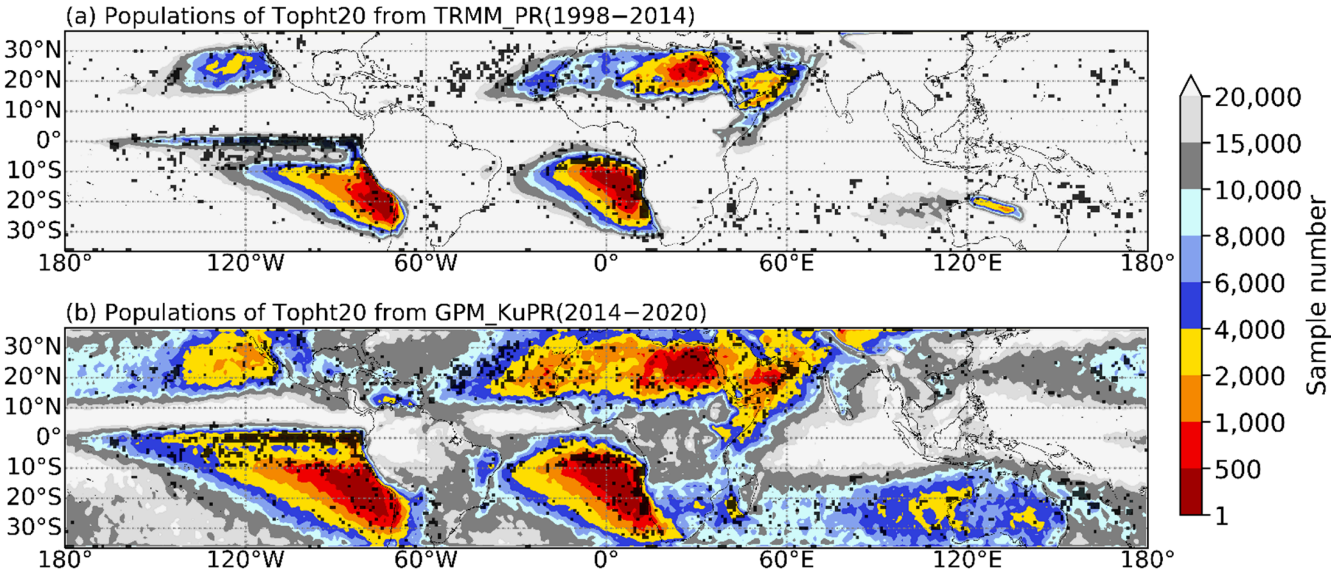

Figure 12. Sample number of Topht20 (shaded) with a spatial grid resolution of 1° × 1° from (**a**) the TRMM_PR (1998–2014) and (**b**) the GPM_KuPR (2014–2020). Grids with a sample >20,000 are not shown. Black points in both panels are the same as in Figure 11c.

4. Discussion

A long-term climatology/time series of precipitation echo-top height has been constructed by combining 23 years (1 January 1998–31 December 2020) of spaceborne radar measurements from the TRMM_PR and the GPM_KuPR. The Topht20s from the TRMM_PR and GPM_KuPR are also consistent from a longer-term climatological perspective, e.g., most of the grids show insignificant differences in the climatological mean Topht20s between the two radars. Only 6% of the grids in the globe exhibit significant discrepancies in Topht20s observed by the two radars. Most of these biased grids are located over regions dominated by shallow convection (Topht20 < 3–4 km). The effects of beam-mismatch from the TRMM_PR and sidelobe clutter from the GPM_KuPR, and non-uniform radar beam filling issue for shallow isolated convection, as well as the insufficient sampling in the arid and convection-suppressed areas, could be responsible for this relatively large discrepancy in the shallow precipitation. Caution should be used when combining observations from the TRMM_PR and GPM_KuPR for the study of shallow precipitation.

5. Conclusions

The consistency of the VPR and echo-top heights between the TRMM_PR and GPM_KuPR satellites has been evaluated. First, VPR and 20-dBZ echo-top heights (Topht20s) have been compared for coincidently observed precipitation events by both radars. The coincident VPR over both convective and stratiform rain types agree well between the two platforms, especially for the VPR of moderate and deep convective events. The coincident Topht20s between the TRMM_PR and GPM_KuPR are highly correlated, with biases within the radar range resolution (0.1–0.2 km). PDFs of Topht20s as a function of height also matched well, e.g., the

statistical characteristics of the bimodal (unimodal) PDF for convective (stratiform) rain were well captured. Second, the latitudinal distributions of Topht20s during the overlapping period are almost a superimposition, especially for the moderate and deep convection in both the tropics and subtropics. The maximum discrepancy in the Topht20 between the two radars occurs in shallow convection.

In conclusion, the analyses have demonstrated the climatological consistency of vertical precipitation structure and convective echo-top heights between the TRMM_PR and GPM_KuPR and provided guidelines in combining the TRMM_PR and GPM_KuPR vertical profiles for long-term climate research on convection.

Author Contributions: L.J. performed the data processing and analysis, and prepared the manuscript; W.X. supervised the analysis, secured funding for this research project, and revised the manuscript. H.C. provided GPM data source and revised the manuscript; N.L. updated the research methodology and revised the manuscript. All authors have read and agreed to the published version of the manuscript.

Funding: This research was supported by the National Natural Science Foundation of China (#41975053), and the Guangdong Provincial Department of Science and Technology, China (#2019QN01G107, #2019ZT08G090). H.C. was supported by the NASA Precipitation Measurement Missions (PMM) program through Interagency NOAA/NASA agreement (#80HQTR20T0046).

Data Availability Statement: The TRMM V8 dataset is available online from the University of Utah (http://atmos.tamucc.edu/trmm/data/trmm/current/level_1/, accessed on 10 April 2022), and the GPM V06A dataset can be accessed from the National Aeronautics and Space Administration (NASA) Global Precipitation Measurement Mission program (https://disc.sci.gsfc.nasa.gov/datasets/GPM_2ADPR_06/summary?keywords=2ADPR, accessed on 10 April 2022). All statistics and visualization are operated with Anaconda Individual Edition Python version 3.8.3 (https://www.anaconda.com/products/individual, accessed on 10 April 2022).

Acknowledgments: All authors acknowledge helps from the Department of Meteorology, University of Utah, and Chuntao Liu from the Department of Physical and Environmental Sciences, Texas A&M Corpus Christi, and the NASA Global Precipitation Measurement program. We appreciate the valuable review comments from three anonymous reviewers.

Conflicts of Interest: The authors declare no conflict of interest.

References

1. Jian, H.-W.; Chen, W.-T.; Chen, P.-J.; Wu, C.-M.; Rasmussen, K.L. The Synoptically-Influenced Extreme Precipitation Systems over Asian-Australian Monsoon Region Observed by TRMM Precipitation Radar. *J. Meteorol. Soc. Jpn. Ser. II* **2021**, *99*, 269–285. [CrossRef]
2. Zhou, Z.; Zhang, Q.; Allen, J.T.; Ni, X.; Ng, C.P. How Many Types of Severe Hailstorm Environments Are There Globally? *Geophys. Res. Lett.* **2021**, *48*, e2021GL095485. [CrossRef]
3. Peterson, M.J.; Lang, T.J.; Logan, T.; Kiong, C.W.; Gijben, M.; Holle, R.; Kolmasova, I.; Marisaldi, M.; Montanya, J.; Pawar, S.D.; et al. New WMO Certified Megaflash Lightning Extremes for Flash Distance (768 km) and Duration (17.01 seconds) Recorded from Space. *Bull. Am. Meteorol. Soc.* **2022**. [CrossRef]
4. Mouri, G.; Shiiba, M.; Hori, T.; Oki, T. Modeling shallow landslides and river bed variation associated with extreme rainfall-runoff events in a granitoid mountainous forested catchment in Japan. *Geomorphology* **2011**, *125*, 282–292. [CrossRef]
5. Wu, C.; Huang, G. Changes in heavy precipitation and floods in the upstream of the Beijiang River basin, South China. *Int. J. Clim.* **2015**, *35*, 2978–2992. [CrossRef]
6. Houze, R.A., Jr.; Rasmussen, K.L.; Zuluaga, M.D.; Brodzik, S.R. The variable nature of convection in the tropics and subtropics: A legacy of 16 years of the Tropical Rainfall Measuring Mission satellite. *Rev. Geophys.* **2015**, *53*, 994–1021. [CrossRef]
7. Tao, W.-K.; Simpson, J.; Lang, S.; McCumber, M.; Adler, R.; Penc, R. An algorithm to estimate the heating budget from vertical hydrometeor profiles. *J. Appl. Meteorol.* **1990**, *29*, 1232–1244. [CrossRef]
8. Liu, C.; Zipser, E.J. Global distribution of convection penetrating the tropical tropopause. *J. Geophys. Res.* **2005**, *110*, D23104. [CrossRef]
9. Liu, N.; Liu, C.; Hayden, L. Climatology and Detection of Overshooting Convection From 4 Years of GPM Precipitation Radar and Passive Microwave Observations. *J. Geophys. Res.* **2020**, *125*, e2019JD032003. [CrossRef]
10. Fromm, M.D.; Servranckx, R. Transport of forest fire smoke above the tropopause by supercell convection. *Geophys. Res. Lett.* **2003**, *30*, 1542. [CrossRef]

11. Groenemeijer, P.; Púčik, T.; Holzer, A.M.; Antonescu, B.; Riemann-Campe, K.; Schultz, D.M.; Kühne, T.; Feuerstein, B.; Brooks, H.E.; Doswell, C.A.; et al. Severe Convective Storms in Europe: Ten Years of Research and Education at the European Severe Storms Laboratory. *Bull. Am. Meteorol. Soc.* **2017**, *98*, 2641–2651. [CrossRef]
12. Houze, R.A.; Wang, J.; Fan, J.; Brodzik, S.; Feng, Z. Extreme Convective Storms Over High-Latitude Continental Areas Where Maximum Warming Is Occurring. *Geophys. Res. Lett.* **2019**, *46*, 4059–4065. [CrossRef]
13. Wuebbles, D.J.; Fahey, D.W.; Hibbard, K.A.; DeAngelo, B.; Doherty, S.; Hayhoe, K.; Horton, R.; Kossin, J.P.; Taylor, P.C.; Waple, A.M.; et al. Executive summary. In *Climate Science Special Report*; Wuebbles, D.J., Fahey, D.W., Hibbard, K.A., Dokken, D.J., Stewart, B.C., Maycock, T.K., Eds.; U.S. Global Change Research Program: Washington, DC, USA, 2017; pp. 12–34. Available online: https://dr.lib.iastate.edu/handle/20.500.12876/5081 (accessed on 10 April 2022).
14. Darden, C.B.; Nadler, D.J.; Carcione, B.C.; Blakeslee, R.J.; Stano, G.T.; Buechler, D.E. Utilizing Total Lightning Information to Diagnose Convective Trends. *Bull. Am. Meteorol. Soc.* **2010**, *91*, 167–176. Available online: https://www.jstor.org/stable/26232859 (accessed on 10 April 2022). [CrossRef]
15. Easterling, D.R.; Kunkel, K.E.; Wehner, M.F.; Sun, L. Detection and attribution of climate extremes in the observed record. *Weather. Clim. Extrem.* **2016**, *11*, 17–27. [CrossRef]
16. Llasat, M.C.; Marcos, R.; Turco, M.; Gilabert, J.; Llasat-Botija, M. Trends in flash flood events versus convective precipitation in the Mediterranean region: The case of Catalonia. *J. Hydrol.* **2016**, *541*, 24–37. [CrossRef]
17. Price, C. Will a drier climate result in more lightning? *Atmos. Res.* **2009**, *91*, 479–484. [CrossRef]
18. Romps, D.M.; Seeley, J.T.; Vollaro, D.; Molinari, J. Projected increase in lightning strikes in the United States due to global warming. *Science* **2014**, *346*, 851–854. [CrossRef]
19. Mohr, K.I.; Zipser, E.J. Defining Mesoscale Convective Systems by Their 85-GHz Ice-Scattering Signatures. *Bull. Am. Meteorol. Soc.* **1996**, *77*, 1179–1190. [CrossRef]
20. Cecil, D.J. Relating Passive 37-GHz Scattering to Radar Profiles in Strong Convection. *J. Appl. Meteorol. Clim.* **2011**, *50*, 233–240. [CrossRef]
21. Liu, C.; Zipser, E.J.; Nesbitt, S.W. Global Distribution of Tropical Deep Convection: Different Perspectives from TRMM Infrared and Radar Data. *J. Climate* **2007**, *20*, 489–503. [CrossRef]
22. Kummerow, C.; Barnes, W.; Kozu, T.; Shiue, J.; Simpson, J. The Tropical Rainfall Measuring Mission (TRMM) Sensor Package. *J. Atmos. Ocean. Technol.* **1998**, *15*, 809–817. [CrossRef]
23. Hou, A.Y.; Kakar, R.K.; Neeck, S.; Azarbarzin, A.A.; Kummerow, C.D.; Kojima, M.; Oki, R.; Nakamura, K.; Iguchi, T. The Global Precipitation Measurement Mission. *Bull. Am. Meteorol. Soc.* **2014**, *95*, 701–722. [CrossRef]
24. Zipser, E.J.; Cecil, D.J.; Liu, C.; Nesbitt, S.W.; Yorty, D.P. Where are the most intense thunderstorms on earth? *Bull. Am. Meteorol. Soc.* **2006**, *87*, 1057–1072. [CrossRef]
25. Xu, W.; Zipser, E.J. Properties of deep convection in tropical continental, monsoon, and oceanic rainfall regimes. *Geophys. Res. Lett.* **2012**, *39*, L07802. [CrossRef]
26. Hamada, A.; Takayabu, Y.N.; Liu, C.; Zipser, E.J. Weak linkage between the heaviest rainfall and tallest storms. *Nat. Commun.* **2015**, *6*, 6213. [CrossRef]
27. Wang, T.; Tang, G. Spatial Variability and Linkage between Extreme Convections and Extreme Precipitation Revealed by 22-Year Space-Borne Precipitation Radar Data. *Geophys. Res. Lett.* **2020**, *47*, e2020GL088437. [CrossRef]
28. Nesbitt, S.W.; Cifelli, R.; Rutledge, S.A. Storm Morphology and Rainfall Characteristics of TRMM Precipitation Features. *Mon. Weather Rev.* **2006**, *134*, 2702–2721. [CrossRef]
29. Liu, C.; Zipser, E.J. The global distribution of largest, deepest, and most intense precipitation systems. *Geophys. Res. Lett.* **2015**, *42*, 3591–3595. [CrossRef]
30. Wang, J.; Houze, J.R.A.; Fan, J.; Brodzik, S.R.; Feng, Z.; Hardin, J.C. The Detection of Mesoscale Convective Systems by the GPM Ku-Band Spaceborne Radar. *J. Meteorol. Soc. Japan. Ser. II* **2019**, *97*, 1059–1073. [CrossRef]
31. Hayden, L.; Liu, C.; Liu, N. Properties of Mesoscale Convective Systems Throughout Their Lifetimes Using IMERG, GPM, WWLLN, and a Simplified Tracking Algorithm. *J. Geophys. Res.* **2021**, *126*, e2021JD035264. [CrossRef]
32. Liu, C.; Zipser, E. Regional variation of morphology of organized convection in the tropics and subtropics. *J. Geophys. Res.* **2013**, *118*, 453–466. [CrossRef]
33. Houze, R.A., Jr.; Wilton, D.C.; Smull, B.F. Monsoon convection in the Himalayan region as seen by the TRMM Precipitation Radar. *Quart. J. Roy. Meteorol. Soc.* **2007**, *133*, 1389–1411. [CrossRef]
34. Liu, C.; Zipser, E.J.; Cecil, D.J.; Nesbitt, S.W.; Sherwood, S. A Cloud and Precipitation Feature Database from Nine Years of TRMM Observations. *J. Appl. Meteorol. Clim.* **2008**, *47*, 2712–2728. [CrossRef]
35. Xu, W. Precipitation and Convective Characteristics of Summer Deep Convection over East Asia Observed by TRMM. *Mon. Weather Rev.* **2013**, *141*, 1577–1592. [CrossRef]
36. Ni, X.; Liu, C.; Zipser, E. Ice Microphysical Properties near the Tops of Deep Convective Cores Implied by the GPM Dual-Frequency Radar Observations. *J. Atmos. Sci.* **2019**, *76*, 2899–2917. [CrossRef]
37. Heymsfield, G.M.; Tian, L.; Heymsfield, A.J.; Li, L.; Guimond, S. Characteristics of Deep Tropical and Subtropical Convection from Nadir-Viewing High-Altitude Airborne Doppler Radar. *J. Atmos. Sci.* **2010**, *67*, 285–308. [CrossRef]
38. Bhat, G.S.; Kumar, S. Vertical structure of cumulonimbus towers and intense convective clouds over the South Asian region during the summer monsoon season. *J. Geophys. Res.* **2015**, *120*, 1710–1722. [CrossRef]

39. Yokoyama, C.; Zipser, E.J.; Liu, C. TRMM-Observed Shallow versus Deep Convection in the Eastern Pacific Related to Large-Scale Circulations in Reanalysis Datasets. *J. Clim.* **2014**, *27*, 5575–5592. [CrossRef]
40. Jiang, H. The Relationship between Tropical Cyclone Intensity Change and the Strength of Inner-Core Convection. *Mon. Weather Rev.* **2012**, *140*, 1164–1176. [CrossRef]
41. Tao, C.; Jiang, H. Global Distribution of Hot Towers in Tropical Cyclones Based on 11-Yr TRMM Data. *J. Clim.* **2013**, *26*, 1371–1386. [CrossRef]
42. Lane, T.P.; Sharman, R.D.; Clark, T.L.; Hsu, H.-M. An Investigation of Turbulence Generation Mechanisms above Deep Convection. *J. Atmos. Sci.* **2003**, *60*, 1297–1321. [CrossRef]
43. Powell, S.W.; Houze, R.A. Evolution of precipitation and convective echo top heights observed by TRMM radar over the Indian Ocean during DYNAMO. *J. Geophys. Res.* **2015**, *120*, 3906–3919. [CrossRef]
44. Xu, W.; Rutledge, S.A. Convective Variability Associated with the Boreal Summer Intraseasonal Oscillation in the South China Sea Region. *J. Clim.* **2018**, *31*, 7363–7383. [CrossRef]
45. Gao, J.; Tang, G.; Hong, Y. Similarities and Improvements of GPM Dual-Frequency Precipitation Radar (DPR) upon TRMM Precipitation Radar (PR) in Global Precipitation Rate Estimation, Type Classification and Vertical Profiling. *Remote Sens.* **2017**, *9*, 1142. [CrossRef]
46. Tang, G.; Wen, Y.; Gao, J.; Long, D.; Ma, Y.; Wan, W.; Hong, Y. Similarities and differences between three coexisting spaceborne radars in global rainfall and snowfall estimation. *Water Resour. Res.* **2017**, *53*, 3835–3853. [CrossRef]
47. Seto, S. Examining the consistency of precipitation rate estimates between the TRMM and GPM Ku-band radars. *Sola* **2022**. advpub. [CrossRef]
48. Takahashi, H.G.; Fujinami, H. Recent decadal enhancement of Meiyu-Baiu heavy rainfall over East Asia. *Sci. Rep.* **2021**, *11*, 13665. [CrossRef]
49. JAXA. TRMM_Product_List_V6_20181004. 2018, Japan Aerospace Exploration Agency, 8. Available online: https://gportal.jaxa.jp/gpr/assets/mng_upload/TRMM_GPMFormat/TRMM_Product_List.pdf (accessed on 10 April 2022).
50. Seto, S.; Iguchi, T. Intercomparison of Attenuation Correction Methods for the GPM Dual-Frequency Precipitation Radar. *J. Atmos. Ocean. Technol.* **2015**, *32*, 915–926. [CrossRef]
51. Iguchi, T.; Seto, S.; Meneghini, R.; Yoshida, N.; Awaka, J.; Le, M.; Chandrasekar, V.; Brodzik, S.; Kubota, T.; Takahashi, N. GPM/DPR Level-2 Algorithm Theoretical Basis Document in V07A. 2021, 238. Available online: https://www.eorc.jaxa.jp/GPM/doc/algorithm/ATBD_DPR_V07A.pdf (accessed on 10 April 2022).
52. Masaki, T.; Iguchi, T.; Kanemaru, K.; Furukawa, K.; Yoshida, N.; Kubota, T.; Oki, R. Calibration of the Dual-Frequency Precipitation Radar Onboard the Global Precipitation Measurement Core Observatory. *IEEE Trans. Geosci. Remote Sens.* **2022**, *60*, 1–16. [CrossRef]
53. Toyoshima, K.; Masunaga, H.; Furuzawa, F.A. Early Evaluation of Ku- and Ka-Band Sensitivities for the Global Precipitation Measurement (GPM) Dual-Frequency Precipitation Radar (DPR). *Sola* **2015**, *11*, 14–17. [CrossRef]
54. JAXA. GPM_data_util_handbook_V6_20181004_E. 2018, Japan Aerospace Exploration Agency: Japan, 115. Available online: https://www.eorc.jaxa.jp/TRMM/documents/PR_algorithm_product_information/doc_pr_v8/GPM_data_util_handbook_V6_20181004_E.pdf (accessed on 10 April 2022).
55. Awaka, J. Early results on rain type classification by the Tropical Rainfall Measuring Mission (TRMM) Precipitation Radar. In Proceedings of the URSI-F Open Symposion on Wave Propagation and Remote Sensing, Aveiro, Portugal, 22–25 September 1998; pp. 143–146. Available online: https://ci.nii.ac.jp/naid/10025262166/en/ (accessed on 10 April 2022).
56. Awaka, J.; Iguchi, T.; Okamoto, K.i. TRMM PR Standard Algorithm 2A23 and its Performance on Bright Band Detection. *J. Meteorol. Soc. Jpn. Ser. II* **2009**, *87A*, 31–52. [CrossRef]
57. Iguchi, T.; Kawamoto, N.; Oki, R. Detection of Intense Ice Precipitation with GPM/DPR. *J. Atmos. Ocean. Technol.* **2018**, *35*, 491–502. [CrossRef]
58. Turk, F.J.; Ringerud, S.E.; Camplani, A.; Casella, D.; Chase, R.J.; Ebtehaj, A.; Gong, J.; Kulie, M.; Liu, G.; Milani, L.; et al. Applications of a CloudSat-TRMM and CloudSat-GPM Satellite Coincidence Dataset. *Remote Sens.* **2021**, *13*, 2264. [CrossRef]
59. Hamada, A.; Takayabu, Y.N. Improvements in Detection of Light Precipitation with the Global Precipitation Measurement Dual-Frequency Precipitation Radar (GPM DPR). *J. Atmos. Ocean. Technol.* **2016**, *33*, 653–667. [CrossRef]
60. Kubota, T.; Iguchi, T.; Kojima, M.; Liao, L.; Masaki, T.; Hanado, H.; Meneghini, R.; Oki, R. A Statistical Method for Reducing Sidelobe Clutter for the Ku-Band Precipitation Radar on board the GPM Core Observatory. *J. Atmos. Ocean. Technol.* **2016**, *33*, 1413–1428. [CrossRef]
61. Takahashi, N.; Iguchi, T. Estimation and correction of beam mismatch of the precipitation Radar after an orbit boost of the tropical rainfall measuring mission Satellite. *IEEE Trans. Geosci. Remote Sens.* **2004**, *42*, 2362–2369. [CrossRef]
62. Kanemaru, K.; Kubota, T.; Iguchi, T. Improvements in the Beam-Mismatch Correction of Precipitation Radar Data After the TRMM Orbit Boost. *IEEE Trans. Geosci. Remote Sens.* **2019**, *57*, 7161–7169. [CrossRef]